Supplementary Materials

Room Temperature Terahertz Electroabsorption Modulation by Excitons in Monolayer Transition Metal Dichalcogenides

Jiaojian Shi[△,†] Edoardo Baldini[△,‡] Simone Latini,[¶] Shunsuke A. Sato,[§,¶] Yaqing Zhang,[†] Brandt C. Pein,[†] Pin-Chun Shen,[‖] Jing Kong,[‖] Angel Rubio,[¶,⊥,#] Nuh Gedik,[‡] and Keith A. Nelson[*,†]

†*Department of Chemistry, Massachusetts Institute of Technology, Cambridge, Massachusetts 02139, United States*

‡*Department of Physics, Massachusetts Institute of Technology, Cambridge, Massachusetts 02139, United States*

¶*Max Planck Institute for the Structure and Dynamics of Matter, Center for Free Electron Laser Science, 22761 Hamburg, Germany*

§*Center for Computational Sciences, University of Tsukuba, Tsukuba 305-8577, Japan*

‖*Department of Electrical Engineering and Computer Science, Massachusetts Institute of Technology, Cambridge, Massachusetts 02139, United States*

⊥*Nano-Bio Spectroscopy Group, Departamento de Fisica de Materiales, Universidad del País Vasco, 20018 San Sebastían, Spain*

#*Center for Computational Quantum Physics, Simons Foundation Flatiron Institute, New York, New York 10010, United States*

E-mail: kanelson@mit.edu

S1. Evaluation of the transient absorption

To evaluate the transient absorption ($\Delta\alpha$) from the measured differential transmittance ($\Delta T_\nu/T_\nu$), we applied a common approach known in the literature.[1] Specifically, we performed a Kramers-Kronig constrained variational analysis[2] to extract the complex dielectric function ($\epsilon = \epsilon_1 + \mathrm{i}\epsilon_2$) from the static transmittance T_ν. The results we obtain are consistent with those reported in previous studies.[3] We then used the dielectric function to obtain the absorbance α, as reported previously.[1] We applied this procedure for all the acquired data at different THz pump field strengths. Finally, at each field strength, we performed a Lorentz analysis of the absorption spectra in order to estimate the parameters for the exciton resonances. The results of the fits are superposed as solid lines over the experimental data in Fig. S6. While the oscillator strength and the exciton peak energy are essentially unchanged under THz excitation, the resonance linewidth undergoes a significant modification with increasing field strength, as shown in Fig. 4(b). Only at the maximum THz field strength, there is a small shift of the A exciton peak energy, which is likely due to the dynamic Franz-Keldysh effect.[4] This observation suggests that at the highest THz field strengths used in our study, the system is entering a non-perturbative regime of excitation. We believe that exciton B may also undergoes a similar spectral shift, but this could be obscured by its broader lineshape. The small shift detected at the maximum THz field strength is incidental to the conclusions of our study.

S2. Theoretical modeling with the Franz-Keldysh effect

The time-resolved results show that the field-induced broadening of the excitonic peaks occurs only during the presence of the THz field. This observation points towards an adiabatic effect which could be interpreted in terms of a static field. We propose that the static Franz-Keldysh effect plays a relevant but indirect role. The textbook manifestation of the Franz-Keldysh effect is the formation of a finite in-gap density of states with an exponential

tail from the electronic bandgap. If such a tail extended far enough to shift and broaden the excitonic resonances, it would result in an asymmetric shape of the A and B excitonic resonances (as the energies of the two resonances are different). Another possibility is that the electric field of the THz pulse induces direct dissociation of the excitons, consequently reducing their lifetimes and broadening their lineshapes. However, according to previous studies,[5,6] the required field magnitude for direct dissociation should be much higher than those utilized in our experiments and the scaling would be different than that observed in our data.

Here, we propose an indirect role of the Franz-Keldysh effect through the modification of particle-hole continuum. Specifically, the Franz-Keldysh effect provides a larger number of particle-hole states below the electronic gap, thus opening additional scattering channels for the excitons and increasing the broadening of their resonances. The scattering of the exciton into a continuum state has to be mediated by the environment (e.g., thermal phonons) and is more favorable if the energy difference between the exciton and the final continuum state is smaller, which is the case for the in-gap states created by the Franz-Keldysh effect.

In the following paragraphs, we analyze the above scenario with a simple model based on the Franz-Keldysh effect and the Redfield equation.

A. Franz-Keldysh effect in 2D systems

Here, we derive the particle-hole continuum density of states, also referred to as the joint density of states, of a two-dimensional material (2D) under the influence of a static electric field. This derivation represents the extension of the Franz-Keldysh effect to the 2D case. Let us start from the time-dependent expression for the density of states as in Eqs. (2) and (3) of Jauho and Johnsen.[4]

$$\rho(\omega, T) = \frac{1}{2\pi} \sum_{\mathbf{k}} \tilde{A}(\mathbf{k}, \omega, T), \tag{1}$$

$$\tilde{A}(\mathbf{k},\omega,T)=\int d\mathbf{r}d\tau e^{iw}\int d\mathbf{p}\times\exp\left\{-i\int_{T-\tau/2}^{T+\tau/2}dt_1\epsilon\left[\mathbf{p}-\mathbf{A}(t_1)\right]\right\}, \tag{2}$$

where $\mathbf{A}(t)$ is the vector potential, and w is defined as

$$w\equiv\tau\omega-\mathbf{r}\cdot\mathbf{k}-\int_{T-\tau/2}^{T+\tau/2}\frac{dt_1}{\tau}\mathbf{r}\cdot\mathbf{A}(t_1). \tag{3}$$

In the following, we consider only a static electric field $\mathbf{E}_0$, which can be described by the following vector potential

$$\mathbf{A}(t)=-\mathbf{E}_0\times(t-T), \tag{4}$$

which, according to Eq. (3) gives

$$w\equiv\tau\omega-\mathbf{r}\cdot\mathbf{k}, \tag{5}$$

and Eq. (2) can be rewritten as

$$\tilde{A}(\mathbf{k},\omega)=\frac{1}{(2\pi)^2}\int_{-\infty}^{\infty}d\tau e^{i\omega\tau}\times\exp\left\{-i\int_{T-\tau/2}^{T+\tau/2}dt_1\epsilon\left[\mathbf{k}-\mathbf{A}(t_1)\right]\right\}. \tag{6}$$

We assume a parabolic band dispersion for particle-hole pairs, which reads

$$\epsilon(\mathbf{k})=\epsilon_g+\frac{1}{2\mu}\mathbf{k}^2, \tag{7}$$

where ϵ_g is the electronic band gap of the crystal, and μ is the reduced electron-hole mass. Under this assumption, the dynamical phase factor in Eq. (6) can be evaluated as

$$\int_{T-\tau/2}^{T+\tau/2}dt_1\epsilon\left[\mathbf{k}-\mathbf{A}(t_1)\right]=\int_{-\tau/2}^{\tau/2}dt_1\epsilon\left[\epsilon_g+\frac{1}{2\mu}\left(\mathbf{k}+\mathbf{E}_0\tau\right)^2\right]=\left(\epsilon_g+\frac{\mathbf{k}^2}{2\mu}\right)\tau+\frac{\mathbf{E}_0^2}{8\mu}\frac{\tau^3}{3}. \tag{8}$$

Inserting Eq. (8) into Eq. (6), we have:

$$\tilde{A}(\mathbf{k},\omega) = \frac{1}{(2\pi)^d}\int_{-\infty}^{\infty} d\tau \exp\left\{-i\left[\left(\epsilon_g + \frac{\mathbf{k}^2}{2\mu} - \omega\right)\tau + \frac{\mathbf{E}_0^2}{8\mu}\frac{\tau^3}{3}\right]\right\} \tag{9}$$

Employing the Airy function, $\mathrm{Ai}(x)$, defined as

$$\mathrm{Ai}(x) = \frac{1}{2\pi}\int_{-\infty}^{\infty} e^{i(t^3/3+tx)} = \frac{1}{2\pi}\int_{-\infty}^{\infty}\cos\left[t^3/3+tx\right] = \frac{1}{\pi}\int_0^{\infty}\cos\left[t^3/3+tx\right], \tag{10}$$

the spectral function $\tilde{A}(\mathbf{k},\omega)$ in Eq. (9) can be rewritten as

$$\tilde{A}(\mathbf{k},\omega) = \frac{1}{(2\pi)^2}\frac{2\pi}{\beta}\mathrm{Ai}\left(\frac{\epsilon_g + \frac{\mathbf{k}^2}{2\mu} - \omega}{\beta}\right), \tag{11}$$

where we introduced β as

$$\beta \equiv \left(\frac{\mathbf{E}_0^2}{8\mu}\right)^{1/3}. \tag{12}$$

The spectral function we just obtained corresponds to Eq. (7) of Ref.[4]

We proceed with the evaluation of the joint density of states by inserting Eq. (11) into Eq. (1),

$$\begin{aligned}\rho^{2D}(\omega) &= \frac{1}{2\pi}\int d\mathbf{k}\frac{1}{(2\pi)^2}\frac{2\pi}{\beta}\mathrm{Ai}\left(\frac{\epsilon_g + \frac{\mathbf{k}^2}{2\mu} - \omega}{\beta}\right) \\ &= \frac{1}{2\pi}\frac{1}{\beta}\int_0^{\infty} dk\cdot k\cdot \mathrm{Ai}\left(\frac{\epsilon_g + \frac{k^2}{2\mu} - \omega}{\beta}\right).\end{aligned} \tag{13}$$

Applying the variable transformation, $x = k^2/2\mu\beta$, Eq. (13) can be rewritten as

$$\begin{aligned}\rho^{2D}(\omega) &= \frac{\mu}{2\pi}\int_0^{\infty} dx\mathrm{Ai}\left(\frac{\epsilon_g - \omega}{\beta} + x\right) \\ &= \frac{\mu}{2\pi}\int_{-\frac{\omega-\epsilon_g}{\beta}}^{\infty} dy\mathrm{Ai}(y),\end{aligned} \tag{14}$$

where we further transformed the integration variable $y = x + (\epsilon_g - \omega)/\beta$.

We can readily see that, in the weak field limit, $\beta \to 0$ ($E_0 \to 0$), the joint density of state expression above becomes a Heaviside step function that is typical of 2D systems

$$\rho^{2D}(\omega) \approx \frac{\mu}{2\pi}\Theta\left(\omega - \epsilon_g\right). \tag{15}$$

Figure S7 shows how the 2D joint density of states is affected by the external electric field with different magnitudes. We can distinguish a typical exponential tail for energies below and an oscillatory behavior above the electronic gap, similar to the three-dimensional case.

B. Theoretical analysis of field enhanced decay of excitons

Here, we derive an expression for the field-induced enhancement of the exciton decay by employing the modified density of states in Eq. (14). We consider a system that consists of a sub-system and a bath described by the Hamiltonian

$$H_{Tot} = H_S + H_B + H_{SB}, \tag{16}$$

where H_S is the subsystem Hamiltonian, H_B is the bath Hamiltonian, and H_{SB} is the coupling between the subsystem and the bath. Furthermore, we assume that the bath consists of a series of harmonic oscillators as

$$H_B = \sum_a \left[\frac{\hat{P}_a^2}{2M_a} + \frac{1}{2}M_a\Omega_a\hat{R}_a^2\right], \tag{17}$$

where M_a is mass of a harmonic oscillator, Ω_a is its eigenfrequency, $\hat{P}_a$ is its momentum operator and $\hat{R}_a$ is its position operator. In this work, we consider the following linear

coupling form for the coupling Hamiltonian H_{SB} as

$$H_{SB} = g \sum_a \hat{A} \otimes \hat{R}_a, \tag{18}$$

where g is a coupling constant and $\hat{A}$ is a sub-system operator.

According to Ref.,[7] under the Born and Markov approximations, one can derive the Redfield equation in the interaction picture,

$$\frac{d\rho(t)}{dt} = -g^2 \sum_a \int_0^t d\tau \left\{ \mathcal{B}_{aa}(\tau) \left[A(t), A(t-\tau)\rho(t) \right] + \text{h.c.} \right\}, \tag{19}$$

with $\mathcal{B}_{aa}(\tau)$ is the correlation function of the a harmonic oscillator, which reads

$$\mathcal{B}_{aa}(\tau) = \text{Tr}\left\{ \hat{R}_a(0) \hat{R}_a(-\tau) \rho_B \right\} = \frac{1}{2M_a\Omega_a} \left[e^{-i\Omega_a\tau} + \frac{2}{e^{\beta\hbar\Omega_a} - 1} \cos\Omega_a\tau \right], \tag{20}$$

where ρ_B is the bath density matrix in thermal equilibrium, and β corresponds to the inverse temperature, $\beta \equiv 1/k_B\mathscr{T}$. Then, we introduce the total correlation function of the bath as

$$\mathcal{B}(\tau) = g^2 \sum_a \mathcal{B}_{aa}(\tau) = \int_0^\infty d\Omega J(\Omega) \left[e^{-i\Omega\tau} + \frac{2}{e^{\beta\hbar\Omega} - 1} \cos(\Omega\tau) \right], \tag{21}$$

where the bath spectral density $J(\Omega)$ is given by

$$J(\Omega) \equiv \sum_a \delta(\Omega - \Omega_a) \frac{g^2}{2M_a\Omega_a}. \tag{22}$$

Employing this bath correlation function, Eq. (21) can be rewritten as

$$\frac{d\rho(t)}{dt} = -\int_0^t d\tau \mathcal{B}(\tau) \left[A(t), A(t-\tau)\rho(t) \right] + \text{h.c.} \tag{23}$$

We then proceed with the evaluation of the population transfer rate from the excitonic state $|e\rangle$ to a final state $|f\rangle$ (a continuum particle-hole state) via the interaction with the

bath as

$$\begin{aligned}
\gamma_f &= \frac{\langle f|\rho(T)|f\rangle - \langle f|\rho(0)|f\rangle}{T} \\
&= -\frac{1}{T}\mathrm{Tr}\left\{|f\rangle\langle f|\int_0^T dt\int_0^t d\tau\mathcal{B}(\tau)\left\{[A(t),A(t-\tau)\rho(t)]+\mathrm{h.c.}\right\}\right\} \\
&\approx -\frac{1}{T}\mathrm{Tr}\left\{|f\rangle\langle f|\int_0^T dt\int_0^\infty d\tau\mathcal{B}(\tau)\left\{[A(t),A(t-\tau)\rho(t)]+\mathrm{h.c.}\right\}\right\}, \qquad (24)
\end{aligned}$$

where, in the last step, we changed integration limits assuming that the period T is much longer than the decay time of the correlation function $\mathcal{B}(\tau)$. We further assume that the system is initially in the exciton state, $\rho(0) = |e\rangle\langle e|$ and that the subsystem-bath coupling is weak. As a result, one can evaluate the leading term of the scattering rate as

$$\begin{aligned}
\gamma_f &\approx -\frac{1}{T}\mathrm{Tr}\left\{|f\rangle\langle f|\int_0^T dt\int_0^\infty d\tau\mathcal{B}(\tau)\left\{[A(t),A(t-\tau)|e\rangle\langle e|]+\mathrm{h.c.}\right\}\right\} \\
&= \int_0^\infty d\tau\mathcal{B}(\tau)|\langle f|A|e\rangle|^2 e^{-i\left(\epsilon_f-\epsilon_e\right)\tau}+c.c., \qquad (25)
\end{aligned}$$

where ϵ_e and ϵ_f are the energy of the exciton and the final state, respectively. In the last line of Eq. (25), we used the definition of the operator $A(t) \equiv e^{iH_S t}Ae^{-iH_S t}$. Inserting Eq. (21) into Eq. (25), the following expression is obtained:

$$\gamma_f = 2\pi|\langle f|A|e\rangle|^2 J(\Omega)\frac{1}{e^{\beta\hbar\Omega}-1}\bigg|_{\hbar\Omega=\epsilon_f-\epsilon_e}, \qquad (26)$$

where $\epsilon_f - \epsilon_e > 0$ is assumed.

By adding contributions from all possible final states, the decay rate of the exciton via the environment can be evaluated as $\gamma = \sum_f \gamma_f$. Further assuming that matrix elements $|\langle f|A|e\rangle|^2$ do not depend on the final states, $|\langle f|A|e\rangle| = \mathcal{M}^2$, one can evaluate the decay rate as

$$\gamma = \sum_f 2\pi\mathcal{M}^2 J(\Omega)\frac{1}{e^{\beta\hbar\Omega}-1}\bigg|_{\hbar\Omega=\epsilon_f-\epsilon_e} = 2\pi\mathcal{M}^2\int_0^\infty d\Omega J(\Omega)n_B(\Omega)\rho_D(\Omega), \qquad (27)$$

where $n_B(\Omega)$ is the Bose-Einstein distribution, $n_B(\Omega) = (e^{\beta\hbar\Omega} - 1)^{-1}$, and the density of states of the final system $\rho_D(\omega)$ is introduced as

$$\rho_D(\omega) = \sum_f \delta(\epsilon_f - \epsilon_e - \omega). \tag{28}$$

A standard assumption for harmonic oscillator bath is to assume an Ohmic spectral density,

$$J(\Omega) = \eta\Omega e^{-\Omega/\Omega_c}, \tag{29}$$

where η is a coupling strength parameter, and Ω_c is the cutoff frequency. Further assuming the high-temperature limit, $\hbar\Omega_c/k_B\mathscr{T} \ll 1$, for the Bose-Einsten distribution, the decay rate in Eq. (27) is described as

$$\gamma = 2\pi\eta k_B \mathscr{T}\mathcal{M}^2 \int_0^\infty d\omega \exp\left[-\frac{\omega}{\Omega_c}\right] \rho_D(\omega). \tag{30}$$

Employing Eq. (14) as the density of states of 2D materials under an electric field, the decay rate γ can be evaluated as

$$\gamma = \frac{\gamma_0}{\Omega_c e^{-\epsilon_e/\Omega_c}} \frac{2\pi}{\mu} \int_0^\infty d\omega e^{-\frac{\omega}{\Omega_c}} \rho^{2D}(\omega), \tag{31}$$

where γ_0 is the intrinsic decay rate without the applied electric field, which is recovered in the limit of $E_0 \to 0$.

Furthermore, if the external field is not strong enough to induce direct ionization, the decay rate of Eq. (31) can be approximated as

$$\gamma \approx \frac{\gamma_0}{\Omega_c e^{-\epsilon_e/\Omega_c}} \frac{2\pi}{\mu} \int_{-\infty}^\infty d\omega e^{-\frac{\omega}{\Omega_c}} \rho^{2D}(\omega) = \gamma_0 \exp\left[\frac{\mathbf{E}_0^2}{8\mu} \frac{1}{3\Omega_c^3}\right]. \tag{32}$$

From this expression we can explicitly evaluate the effect of the external electric field on

the excitonic linewidth.

Finally, from Eq. (32), one can clearly see that in the weak field limit the enhancement of the decay rate is proportional to the square of the electric field strength,

$$\gamma = \gamma_0 \exp\left[\frac{\mathbf{E}_0^2}{8\mu}\frac{1}{3\Omega_c^3}\right] \approx \gamma_0\left[1 + \frac{\mathbf{E}_0^2}{8\mu}\frac{1}{3\Omega_c^3}\right], \tag{33}$$

This finding is consistent with the experimental evidence that the broadening is linear in the field intensity as shown in the main text.

To evaluate the transient absorption and the exciton linewidth in Fig. 4(c,d) in the main text with Eq. (33), we set the intrinsic excitonic linewidth γ_0 to $\gamma_0^A = 67$ meV and $\gamma_0^B = 157$ meV for the A and B excitons, obtained from Lorentz fits of the absorption spectra in equilibrium. Furthermore, for the best fits to experimental results, the cutoff frequencies Ω_c were set to $\Omega_c^A = 49$ meV$/\hbar$ and $\Omega_c^B = 66$ meV$/\hbar$ for the A and B excitons, respectively. We used the common excitonic mass $\mu = 0.24m_e$ for the A and B excitons.[8]

C. Alternative scenarios behind the observed exciton broadening.

In this paragraph, we consider other mechanisms that can contribute to the exciton broadening. The main observation is that the broadening occurs only during the photoexcitation process and it follows the time profile of the THz electric field (< 1 ps). This behavior allows us to readily exclude all the dissipative phenomena that can occur upon photoexcitation of a semiconductor, as these phenomena give rise to responses that last for tens or hundreds of ps. They include THz-activated defect-site scattering,[9–11] defect-assisted Auger scattering, THz-driven exciton generation via either direct valence-to-conduction band or trapped-carrier liberation, and impulsive dephasing due to exciton-exciton scattering. Concerning the last process, we note that the density of excitons produced by our probe light is extremely low ($< 10^{10}$ cm^{-2}), so most excitons will be too far apart to interact significantly with each other. Therefore, we believe that the mechanism proposed in the previous para-

graphs, based on the Franz-Keldysh effect, is the microscopic effect governing the observed change in the exciton coherent lifetime.

S3. Evaluation of the electro-optic coefficients

In this section, we provide an estimate of the electro-optic coefficients characterizing our monolayer MoS_2 film under the influence of intense THz fields. When irradiating the material with a THz field strength of 420 kV/cm, near 1.90 eV we observe that the real part of the refractive index is modulated by ∼2.2% (Fig. S8). From this value, we can extract the electro-optic coefficient r_{ij} by using the relation $\Delta(1/n^2)_i = \sum_j r_{ij}E_j$, where E_j is the applied electric field and i, j represents x, y and z. Formally, r_{ij} is a tensor. However, in our experiment, we can simplify it to a scalar value r_{eff} by considering that our monolayer MoS_2 film has randomly oriented domains.[12] Since the electric field screening needs to be taken into account in the practical performance of a phase modulator, the value of the (quasi-static) dielectric permittivity ϵ_{DC} becomes an important parameter. Therefore, the performance of a material is measured through the unitless quantity $n^3 r_{eff}/\epsilon_{DC}$.[12] Due to the 2D confinement in the monolayer limit, the value of ϵ_{DC} in MoS_2 is several times larger than that of traditional ferroelectric electro-optic materials. Thus, in an exciton-based electro-optic modulator made out of monolayer MoS_2, the phase modulation capability is much higher than that offered by traditional materials used in electro-optical modulators. For example, evaluating $n^3 r_{eff}/\epsilon_{DC}$ at the He-Ne laser wavelength of 633 nm yields a factor of 5 compared to other materials (see Fig. S9). At 650 nm, the increase would be by more than an order of magnitude ($n^3 r_{eff}/\epsilon_{DC} = 150$). The time evolution of the THz-induced modulation of the excitons in MoS_2 also demonstrates that an exciton-based electro-optic modulator made out of this material possesses an ultrabroad bandwidth of several THz. Similar conclusions can be drawn when considering the THz-induced modulation of the absorption coefficient, which is relevant for the development of electroabsorption modulators. In an experiment utilizing the

transmission geometry like ours, the electroabsorption performance of a material subjected to in-plane electric field can be characterized by the absorption modulation depth. At a field strength of 420 kV/cm, monolayer MoS_2 shows switching from 89.58% transmission to 90.48% around 1.90 eV, which corresponds to an absorption modulation depth around 0.05 dB/nm.

Author Contributions

△ These authors contributed equally to this work.

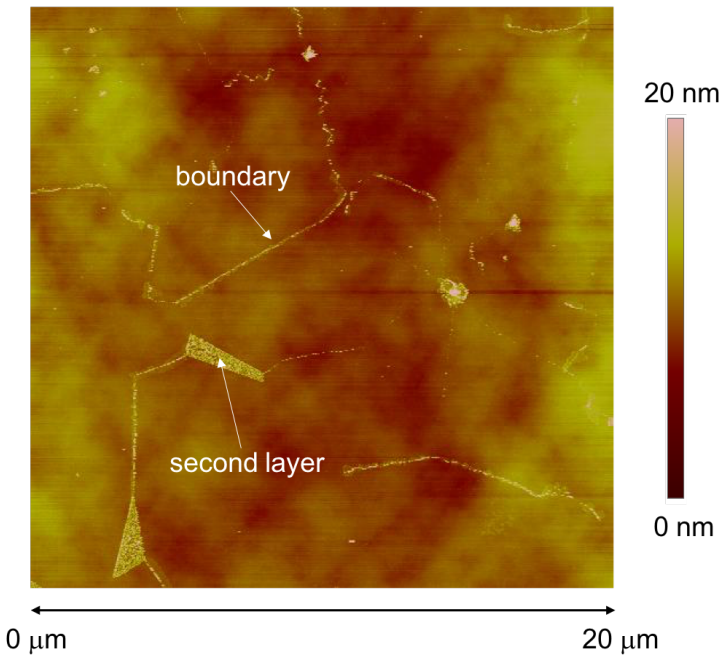

Figure S1: Atomic force microscope image of the surface of CVD-grown MoS_2. The imaged region is 20 μm wide and the color bar refers to the surface roughness. We estimate the domain size in our sample to be 5-10 μm on average. A boundary between two domains and a second layer are indicated. The probe spot size is approximately 50 μm. Therefore, our signal is an averaged response of multiple domains.

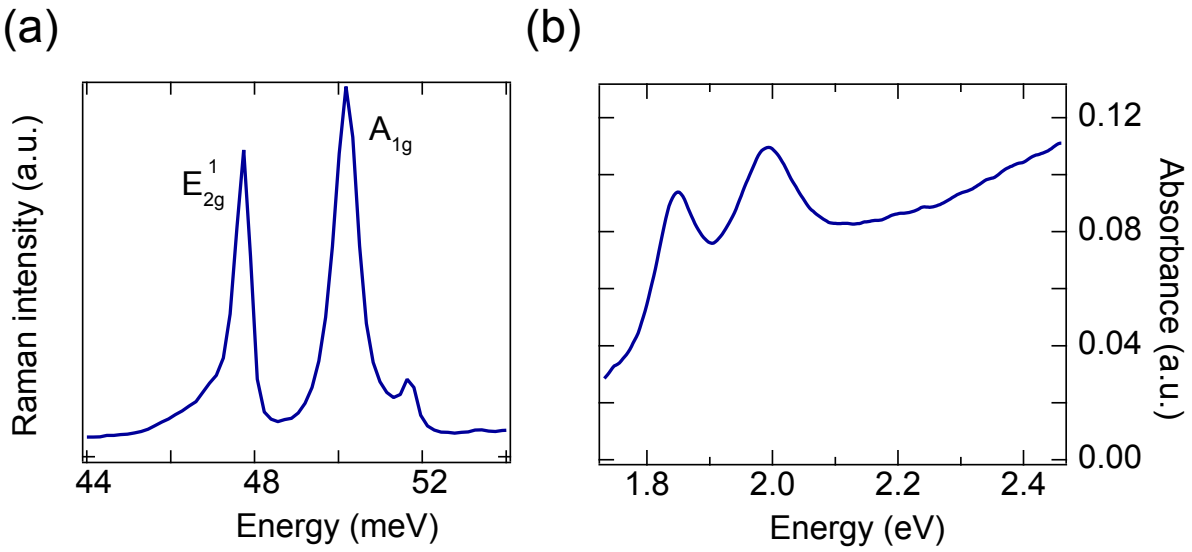

Figure S2: (a) Spontaneous Raman scattering spectrum of the sample. The difference between the energies of the E^1_{2g} and A_{1g} phonons indicates that the sample is a monolayer. (b) Room temperature steady-state absorption spectrum of monolayer MoS_2 showing the A and B exciton peaks.

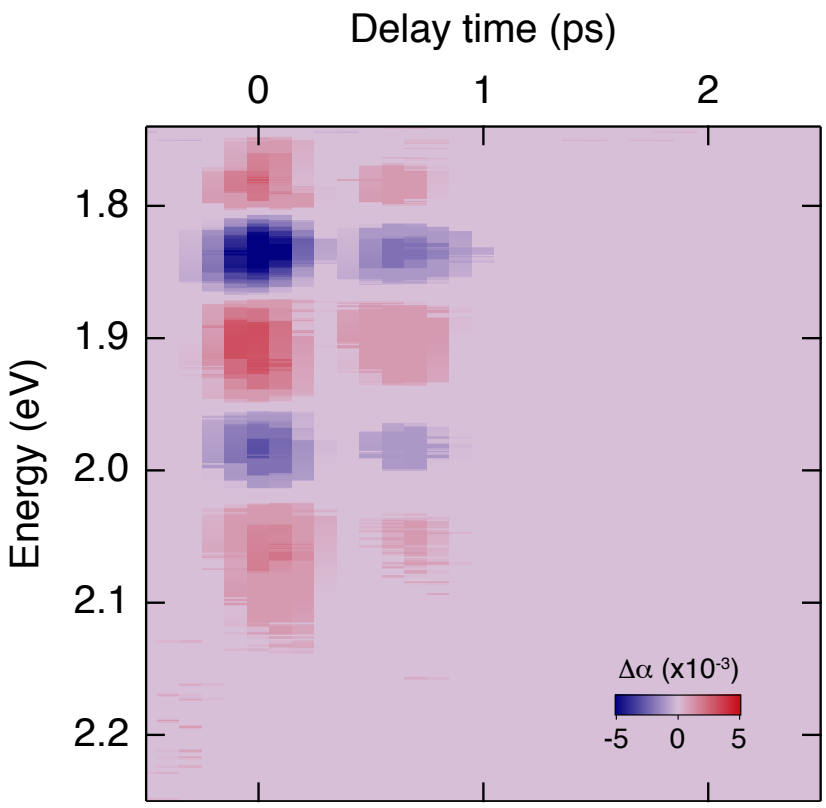

Figure S3: Color-coded map of the differential absorption ($\Delta\alpha$) as a function of the probe photon energy and the time delay between pump and probe. The map shows that no pump-probe signal is present after the THz excitation pulse is over.

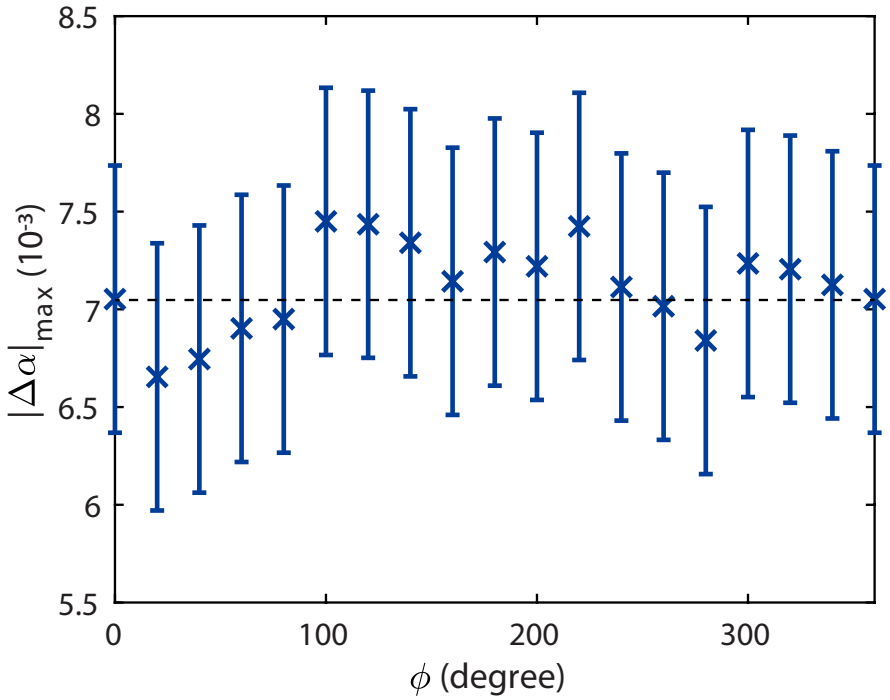

Figure S4: Peak signal $|\Delta\alpha|_{max}$ as a function of the white light probe polarization angle ϕ (while keeping the THz polarization direction fixed). The data presented in the paper are obtained by using a horizontally-polarized white light probe beam and a vertically-polarized THz pump beam. The error bars are measured by the deviation of multiple traces of $\Delta\alpha$ spectrum obtained. We observed no dependence of the signal on the polarization angle.

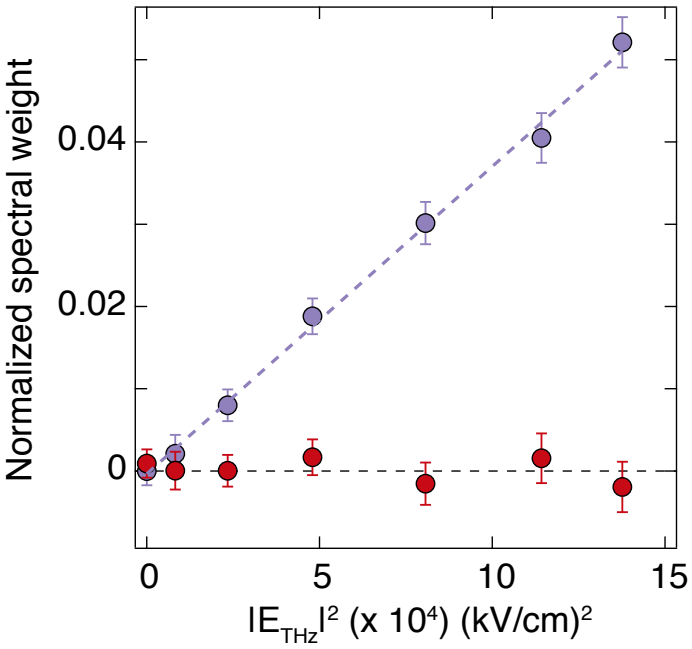

Figure S5: Quantitative analysis of the measured spectra in Fig. 4(a). The red data points are the values of the transient absorption areas normalized to zero-field absorbance area. The violet data points are the absolute values of the transient absorption areas (from 1.73-2.25 eV) normalized to the zero-field absorbance area. The vertical error bars are based on the experimental uncertainties given by the standard deviations from ten datasets taken under the same experimental conditions.

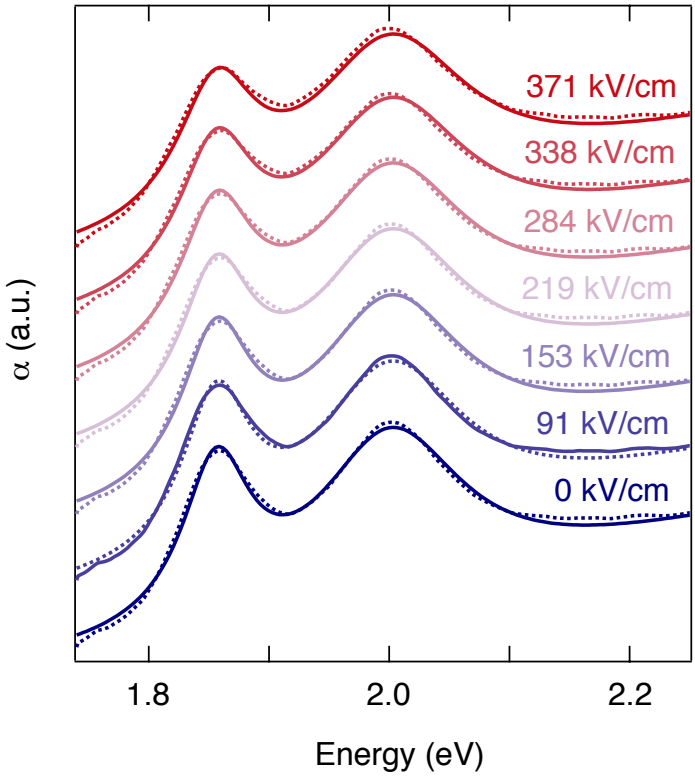

Figure S6: Comparison between the experimental absorption data (dotted lines) and the results of a phenomenological fit (solid lines) at different THz field strengths. The fit function comprises two Lorentz oscillators centered around excitons A and B, as well as a high-energy Lorentz oscillator whose parameters remain fixed at every THz field strength.

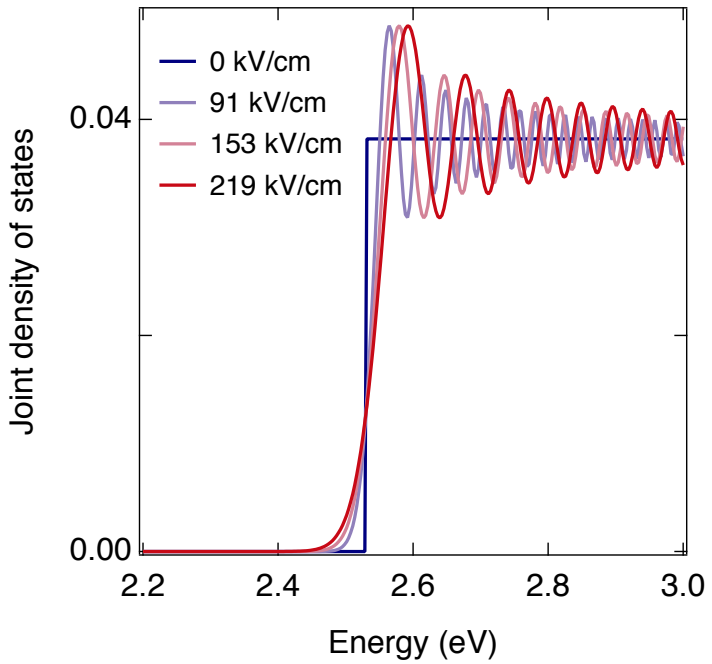

Figure S7: Joint density of states of a 2D crystal under the influence of a static electric field with each of the values indicated. The bands are assumed to have a parabolic energy-momentum dispersion relation. The solid blue line shows the bandgap energy.

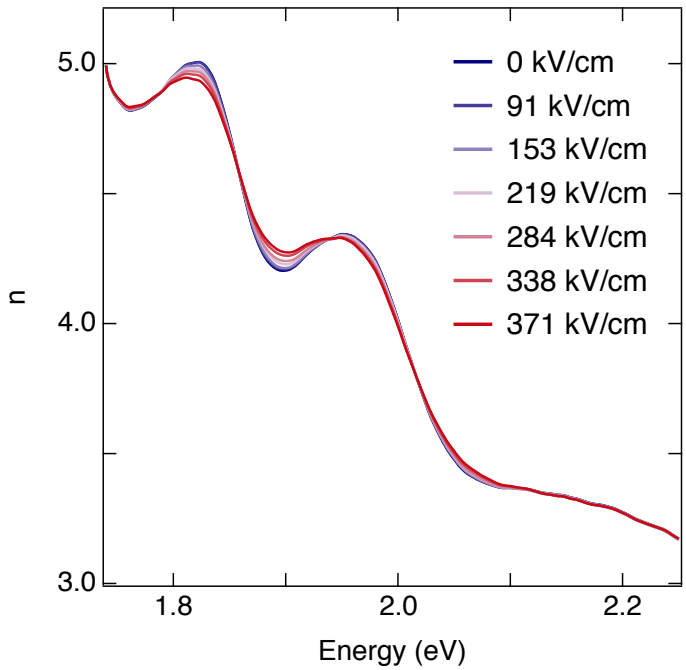

Figure S8: Real part of the refractive index of MoS_2 at zero pump-probe delay plotted in equilibrium (blue trace) and upon excitation with the THz field. The strength of the field is indicated in the label. The maximum variation obtained around 1.90 eV is $\sim$2.2% upon application of a THz field of 420 kV/cm.

Material	Max EO Coefficient (pm/V)	Max Refractive Index	$n^3 r_{eff}$ (pm/V)	$n^3 r_{eff}/\epsilon_{DC}$ (pm/V)
Potassium dihydrogen phosphate, KH_2PO_4	$r_{63} = 10.5$	$n_o = 1.514$ @$0.55\mu m$	36	1.4
Lithium niobate, $LiNbO_3$	$r_{42} = 32.6$	$n_o = 2.3410$ @$0.5\mu m$	418	14
Zinc telluride, ZnTe	$r_{41} = 4.0$	$n_o = 2.99$ @$0.63\mu m$	107	10.3
Barium titanate, $BaTiO_3$	$r_{42} = 1640$	$n_o = 2.488$ @$0.51\mu m$	25257	10.9
Monolayer MoS_2	$\bar{r} \approx 14$	$n \approx 4.9$ @$0.63\mu m$	≈ 1650	≈ 50

Figure S9: Comparison between the electro-optic properties of several materials and those of monolayer MoS_2.

References

(1) Sie, E. J.; Frenzel, A. J.; Lee, Y.-H.; Kong, J.; Gedik, N. Intervalley biexcitons and many-body effects in monolayer MoS_2. *Phys. Rev. B* **2015**, *92*, 125417.

(2) Kuzmenko, A. B. Kramers–Kronig constrained variational analysis of optical spectra. *Rev. Sci. Instr.* **2005**, *76*, 083108.

(3) Li, Y.; Chernikov, A.; Zhang, X.; Rigosi, A.; Hill, H. M.; van der Zande, A. M.; Chenet, D. A.; Shih, E.-M.; Hone, J.; Heinz, T. F. Measurement of the optical dielectric function of monolayer transition-metal dichalcogenides: MoS_2, $MoSe_2$, WS_2, and WSe_2. *Phys. Rev. B* **2014**, *90*, 205422.

(4) Jauho, A. P.; Johnsen, K. Dynamical Franz-Keldysh effect. *Phys. Rev. Lett.* **1996**, *76*, 4576–4579.

(5) Haastrup, S.; Latini, S.; Bolotin, K.; Thygesen, K. S. Stark shift and electric-field-induced dissociation of excitons in monolayer MoS_2 and h BN/MoS_2 heterostructures. *Phys. Rev. B* **2016**, *94*, 041401.

(6) Massicotte, M.; Vialla, F.; Schmidt, P.; Lundeberg, M. B.; Latini, S.; Haastrup, S.; Danovich, M.; Davydovskaya, D.; Watanabe, K.; Taniguchi, T. Dissociation of two-dimensional excitons in monolayer WSe_2. *Nat. Commun.* **2018**, *9*, 1633.

(7) Lidar, D. A. Lecture notes on the theory of open quantum systems. *arXiv:1902.00967* **2019**,

(8) Haastrup, S.; Strange, M.; Pandey, M.; Deilmann, T.; Schmidt, P. S.; Hinsche, N. F.; Gjerding, M. N.; Torelli, D.; Larsen, P. M.; Riis-Jensen, A. C.; Gath, J.; Jacobsen, K. W.; Mortensen, J. J.; Olsen, T.; Thygesen, K. S. The Computational 2D Materials Database: high-throughput modeling and discovery of atomically thin crystals. *2D Materials* **2018**, *5*, 042002.

(9) Hoffmann, M. C.; Hebling, J.; Hwang, H. Y.; Yeh, K.-L.; Nelson, K. A. Impact ionization in InSb probed by terahertz pump—terahertz probe spectroscopy. *Phys. Rev. B* **2009**, *79*, 161201.

(10) Liu, M.; Hwang, H. Y.; Tao, H.; Strikwerda, A. C.; Fan, K.; Keiser, G. R.; Sternbach, A. J.; West, K. G.; Kittiwatanakul, S.; Lu, J.; Wolf, S. A.; Omenetto, F. G.; Zhang, X.; Nelson, K. A.; Averitt, R. D. Terahertz-field-induced insulator-to-metal transition in vanadium dioxide metamaterial. *Nature* **2012**, *487*, 345–348.

(11) Fan, K.; Hwang, H. Y.; Liu, M.; Strikwerda, A. C.; Sternbach, A.; Zhang, J.; Zhao, X.; Zhang, X.; Nelson, K. A.; Averitt, R. D. Nonlinear Terahertz Metamaterials via Field-Enhanced Carrier Dynamics in GaAs. *Phys. Rev. Lett.* **2013**, *110*, 217404.

(12) Boyd, R. W. *Nonlinear Optics*; Elsevier, 2007.